J. Fluid Mech. (2013), *vol.* 736, *pp.* 130–149.
doi:10.1017/jfm.2013.535

Transient dispersion regimes

Rusty C. Holleman† and Mark T. Stacey

Department of Civil and Environmental Engineering, University of California Berkeley, Berkeley, CA 94720, USA

(Received 12 March 2013; revised 26 August 2013; accepted 4 October 2013; first published online 1 November 2013)

Characterizing scalar dispersion is a key concern in a wide variety of applications, including both steady-state and time-dependent studies of wastewater outfalls, salinity distribution in estuaries, and the spreading of pollutants from industrial spills. As the size of a scalar plume grows with respect to the size of the containing water body, the effective dispersion varies, from the well-known $\sigma_x^2 \sim t^3$ behaviour for a plume enveloped in a region of linear shear, to the $\sigma_x^2 \sim t$ behaviour at the limit of a laterally well-mixed plume. We introduce an additional regime in which the plume extends across the full range of the available shear, but is not significantly affected by the lateral bounds of the water body. Through an analytic treatment we show that this regime exhibits a $\sigma_x^2 \sim t^2$ behaviour, independent of lateral mixing coefficient. Particle tracking results in an idealized, tidal channel–shoal basin demonstrate this regime as particle clouds straddle the channel–shoal interface. Quantitative analysis of spatial moments as plumes transition between regimes show good correlation between the observed parameters and parameters predicted by the analytic framework.

Key words: geophysical and geological flows, mixing and dispersion, shallow water flows

1. Introduction

Scalar dispersion, in the most general sense, describes any of a numerous set of physical processes by which features of the flow lead to the spreading out of a scalar species. When considered in Fickian terms the effective dispersion rate is often much greater than the molecular diffusion rate. This rate of spreading is often of fundamental interest in a wide range of applications. In environmental flows, questions related to spatial distributions of nutrient abundance, the spreading of algal blooms, larval transport, and the zone of influence of engineered sources such as wastewater treatment outfalls all trace back to questions of scalar dispersion. In ocean flows dispersion rates are essential for understanding the mixing effects of eddies, formation and breakdown of patches of heightened biological activity, and the mixing action of passing and breaking internal waves (Young, Rhines & Garrett 1982).

Of particular relevance to riverine and estuarine environments is the case of linear shear dispersion, also known as Taylor dispersion due to the first mathematical analysis of Taylor (1953). Given the primary application to estuarine and riverine systems, we will use the term longitudinal to refer to the along-flow axis of the domain (x), and the term lateral to refer to the perpendicular horizontal axis (y).

† Email address for correspondence: holleman@berkeley.edu

Taylor demonstrated that lateral gradients in the longitudinal velocity interacting with lateral diffusion leads to Fickian longitudinal dispersion, albeit with a highly amplified dispersion coefficient. Though the original analysis was targeted at laminar pipe flow, subsequent work in Taylor (1954) and Aris (1956) expanded the analysis to cover a broad range of domains under both laminar and turbulent conditions, summarized in Fischer *et al.* (1979). Central to Taylor's analysis and many subsequent works is the description of dispersion in terms of the growth of the second central moment of the tracer distribution, σ_x^2, equivalently labelled the spatial variance. In the common Fickian model in which scalar flux is proportional to the concentration gradient, σ_x^2 grows with a linear dependence in time $\sigma_x^2 \approx 2K_x t$, with longitudinal dispersion coefficient K_x.

Scalar dispersion in environmental flows may result from the combined action of multiple dispersive processes, such as turbulent mixing, flow asymmetries giving rise to tidal pumping (Stommel & Farmer 1952), tidal trapping (Okubo 1973), and various interactions of velocity shear in one direction with dispersion in an orthogonal direction. The mixing due to these often complex dispersive processes is at least superficially similar to the homogenizing effects of Fickian diffusion, and Fickian models are often used to describe the bulk mixing effects. However, the underlying processes do not necessarily obey a Fickian model (Feng, Cheng & Xi 1986), and at short time scales plume spreading may significantly depart from the Fickian description. These departures from the Fickian model are often termed *anomalous diffusion*, and when considered in terms of a power law relating tracer variance and time, $\sigma_x^2 \sim t^\beta$; the term *subdiffusion* indicates $\beta < 1$ and *superdiffusion* indicates $\beta > 1$ (Young & Jones 1991).

Aris (1956) presented a general framework for evaluating shear dispersion, showing that lateral diffusion coupled with lateral shear in the longitudinal velocity leads to longitudinal dispersion with a Fickian behaviour at asymptotically long time scales. Saffman (1962) extended the analysis of Aris to the case of a plume released at ground level into a semi-infinite shear layer above the plane of the ground, showing that in such a case the variance grows with a cubic dependence on time compared to the linear dependence of Taylor's and Aris' scenarios. Barton (1983) refined the analysis of Aris, clarifying the mathematical assumptions of the analysis, and for a broad subset of flows presented a method for distilling the partial differential equations (PDEs) into a simpler set of ordinary differential equations (ODEs). Solving the more tractable set of ODEs leads to analytic solutions, valid at all time scales, for the moments of a scalar cloud. In introducing considerable mathematical rigour, the approaches of Barton become difficult to apply to environmental flows. For example, while scaling analyses may easily reach the results of Saffman (1962), a semi-infinite flow is incompatible with the approach of Barton (1983), such that one could not arrive at a relationship directly describing the cubic time dependence in unbounded, constant-shear cases. Scaling laws and corresponding qualitative regimes are quite helpful and broadly applied in understanding environmental flows where the precise global flow field may not be known, which in turn motivates the more schematic methods described below. Other recent dispersion mechanism studies include Spydell & Feddersen (2012), considering shear dispersion in a laterally bounded flow but with a non-zero Lagrangian time scale, demonstrating that a non-zero Lagrangian time scale can increase the dispersion coefficient.

The present work is concerned with three regimes of shear dispersion in environmental flows and the transitions there between. For simplicity, the analysis is focused on cases of constant diffusivity, though preliminary investigation of cases

with variable diffusivity have found similar behaviours to the constant-diffusivity case. The initial shear dispersion regime is essentially that described by Saffman (1962), among others, in which a constant-shear velocity profile completely envelops the scalar plume. As the plume expands laterally the range of velocities sampled by the parcels within the plume also increases, leading to an ever-increasing velocity scale associated with the longitudinal dispersion. The straining of the plume by this ever-increasing velocity scale has been shown to result in cubic-in-time variance growth, $\sigma_x^2 \sim t^3$, and will generally be referred to as the 'cubic' regime.

A second regime, introduced more fully in § 2, describes the variance growth of a plume which is not bounded in the lateral direction, but for which the range of velocities sampled by its parcels is essentially constant in time. Schematically this could correspond to a narrow (relative to the lateral extent of the plume) shear layer separating two regions of smaller velocity gradients. Physically, a plume may experience such a flow when the discrete spatial features leading to velocity gradients are large compared to plume extent. One particular example is the geometry of a channel–shoal basin, in which shear is maximal over the sloping region joining the channel and shoal, with comparatively little shear in the channel or shoals. A simple scaling approach to this scenario starts with a plume centred on a shear layer with velocity $+U$ to one side of the shear layer and $-U$ to the other side. The centroid of the plume is stationary and the longitudinal variance a function of the typical displacement Δx of a parcel. While on a particular side of the shear layer, $\Delta x \sim \pm Ut$ and $\sigma_x^2 \sim U^2t^2$. The variance growth is then $\mathrm{d}\sigma_x^2/\mathrm{d}t \sim U^2t^2/T$, where T is the characteristic time for a parcel to return to the shear layer. T scales with the lateral size of the plume as $T \sim \sigma_y^2/K_y$, and in the absence of lateral boundaries $\sigma_y^2 \sim K_y t$, leading to an overall scaling $\mathrm{d}\sigma_x^2/\mathrm{d}t \sim U^2t$ or $\sigma_x^2 \sim U^2t^2$. The application of the Aris method of moments to this flow in § 2 supports this scaling and provides the exact coefficients of proportionality.

In the case of a plume subject to shear but also constrained by lateral boundaries, the variance growth asymptotes to the linear shear dispersion limit $\sigma_x^2 \sim t$ after a time sufficient for the plume to become laterally well-mixed. Only in this final regime does the plume assume a Fickian behaviour.

Section 3 moves to the inverse problem of taking a time series of spatial moments describing the evolution of a plume and estimating the relative importance and parameters of each dispersion regime. Following a description of the inverse problem, idealized flows and plume releases, described in § 4, serve as a test bed for the inverse problem.

2. Analytic derivation

Following the approach of Aris (1956), the advection–diffusion equation can be transformed into an evolution equation for the spatial moments of the scalar distribution. The derivations of this section assume a rectangular channel aligned with the x-axis, with lateral coordinate $y \in [-B/2, B/2]$ and vertical coordinate $z \in [-H, 0]$. Define the pth moment in x for a filament extending along a given line of constant y and z as $c_p(y, z, t)$:

$$c_p(y, z, t) \equiv \int_{-\infty}^{\infty} x^p C(x, y, z, t)\, \mathrm{d}x. \tag{2.1}$$

The pth moment of the overall scalar cloud, m_p, is then defined as the integral of c_p over the cross-section of the channel:

$$m_p(t) \equiv \int_{-B/2}^{B/2} \left[\int_{-H}^{0} c_p(y, z, t)\, \mathrm{d}z \right] \mathrm{d}y. \tag{2.2}$$

Assuming a constant but anisotropic diffusivity described completely by the axis-aligned diffusivities K_x, K_y and K_z, lateral and vertical velocities equal to zero, and along-channel velocity $u = u(y, z)$, the advection–diffusion equation can be written

$$\frac{\partial C}{\partial t} + u\frac{\partial C}{\partial x} = K_x \frac{\partial^2 C}{\partial x^2} + K_y \frac{\partial^2 C}{\partial y^2} + K_z \frac{\partial^2 C}{\partial z^2}. \tag{2.3}$$

Equation (2.3) is then multiplied by x^p and integrated over $x \in (-\infty, \infty)$ to get

$$\int_{-\infty}^{\infty} \left(x^p \frac{\partial C}{\partial t} + u x^p \frac{\partial C}{\partial x} \right) \mathrm{d}x = \int_{-\infty}^{\infty} \left(K_x x^p \frac{\partial^2 C}{\partial x^2} + K_y x^p \frac{\partial^2 C}{\partial y^2} + K_z x^p \frac{\partial^2 C}{\partial z^2} \right) \mathrm{d}x. \tag{2.4}$$

Pulling the time derivative outside the spatial integral and rearranging the advection term leads to

$$\begin{aligned} &\frac{\partial}{\partial t} \left[\int_{-\infty}^{\infty} x^p C\, \mathrm{d}x \right] + u \int_{-\infty}^{\infty} \left[\frac{\partial}{\partial x}(x^p C) - p x^{p-1} C \right] \mathrm{d}x \\ &\quad = K_x \int_{-\infty}^{\infty} x^p \frac{\partial^2 C}{\partial x^2}\, \mathrm{d}x + K_y \int_{-\infty}^{\infty} x^p \frac{\partial^2 C}{\partial y^2}\, \mathrm{d}x + K_z \int_{-\infty}^{\infty} x^p \frac{\partial^2 C}{\partial z^2}\, \mathrm{d}x. \end{aligned} \tag{2.5}$$

Applying the boundary conditions that C and its derivatives approach zero as $x \to \pm\infty$, (2.5) can be further simplified and expressed in terms of c_p, c_{p-1} and c_{p-2} as

$$\frac{\partial c_p}{\partial t} - upc_{p-1} = K_x p(p-1)c_{p-2} + K_y \frac{\partial^2}{\partial y^2} c_p + K_z \frac{\partial^2}{\partial z^2} c_p. \tag{2.6}$$

Define an initial condition for the scalar distribution $C(\boldsymbol{x}, t = 0) \equiv C_0(\boldsymbol{x})$ from which $c_{p,0}(y, z)$ can be directly evaluated, and Neumann boundary conditions of zero flux at the y and z boundaries: $K_{ij}(\partial C/\partial x_i)\hat{n}_j|_{\delta\Omega} = 0$, where $\delta\Omega$ denotes the boundaries of the domain, and $\hat{\boldsymbol{n}}$ the unit vector normal to the boundary. Over the cross-section, the lateral and vertical diffusion integrate to zero, such that substituting the definition of the moment m_p, we arrive at an evolution equation for arbitrary moments,

$$\frac{\mathrm{d}m_p}{\mathrm{d}t} = p\overline{uc_{p-1}} + K_x p(p-1)m_{p-2}, \tag{2.7}$$

where the overbar denotes integration over the cross-section. As a final step, if we choose the coordinate reference frame such that $m_1 = 0$ for all time, i.e. the reference frame of the centroid of the distribution, the longitudinal spatial variance of the plume may then be described by

$$\frac{\mathrm{d}\sigma_x^2}{\mathrm{d}t} = \frac{1}{m_0}\frac{\mathrm{d}m_2}{\mathrm{d}t}. \tag{2.8}$$

2.1. *Linear and cubic time dependence*

Aris (1956) developed the above method and applied it to the case of a channel with an arbitrary lateral velocity profile $u = u(y)$. Taking the simplest shear velocity

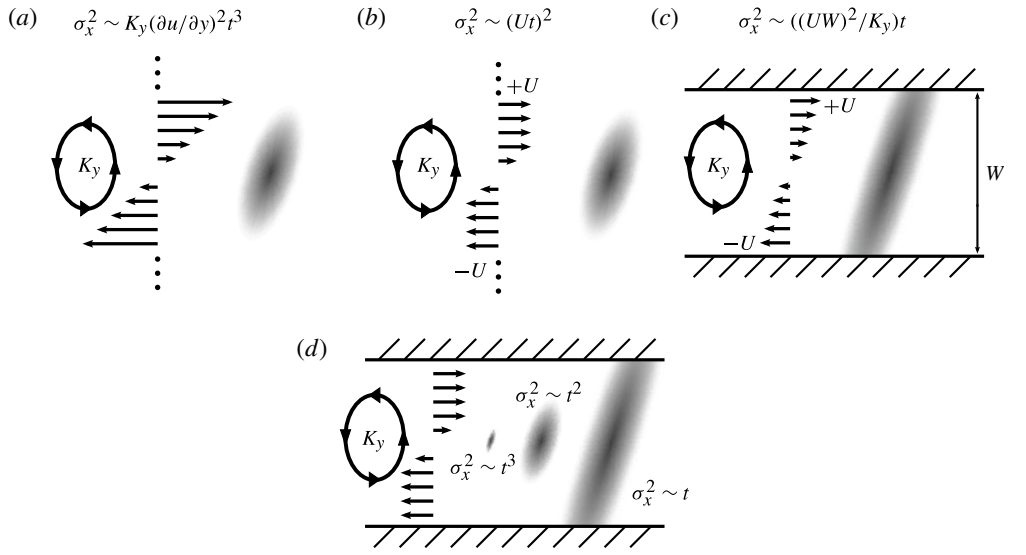

FIGURE 1. Schematic of the three dispersion regimes: (*a*) unbounded shear; (*b*) finite shear, unbounded flow; (*c*) bounded flow; and (*d*) the transitions.

profile, a linear profile with constant shear $S = \partial u/\partial y$, $u = Sy$, with lateral boundaries at $y = \pm W/2$ (illustrated in figure 1*c*), the spatial variance is described by

$$\frac{\mathrm{d}\sigma_x^2}{\mathrm{d}t} = \frac{W^4 S^2}{60 K_y} + 2K_x, \tag{2.9}$$

where σ_x^2 has a linear time dependence: the familiar shear dispersion. If the lateral boundaries are absent but the constant-shear velocity profile is retained (figure 1*a*), the evolving spatial variance is instead described by

$$\frac{\mathrm{d}\sigma_x^2}{\mathrm{d}t} = 2K_y S^2 t^2 + 2K_x, \tag{2.10}$$

such that σ_x^2 has a cubic time dependence (Saffman 1962).

2.2. *Quadratic time dependence*

In the linear case described above both the velocity range and the lateral domain are bounded, leading to a linear growth rate. The cubic case has an unbounded velocity range as well as a lack of lateral boundaries, and the method of moments predicts a cubic time dependence. At a qualitative level, a scenario in which exactly one of the velocity range or lateral boundaries is finite would be expected to yield a quadratic time dependence. Construction of a finite-width channel with an infinite range of velocities is distinctly non-physical, but an unbounded channel with finite shear (figure 1*b*) is well-posed and potentially physical, such as the limiting case of a plume which is large relative to local variation in the velocity field but small relative to the width of the channel. We next apply the method of moments to the scenario of an infinitely wide domain with a finite velocity range. In order to avoid introducing an additional length scale into the model corresponding to the thickness of the shear layer, we impose an infinitely thin shear layer, with velocity field $u(y, z) = U\mathrm{sgn}(y)$, where U is a constant velocity scale.

The zeroth per-filament moment c_0 is purely a function of lateral diffusion and takes the form of a simple Gaussian distribution:

$$c_0(y,t) = \frac{m_0}{H\sqrt{4\pi K_y t}} \exp\left(-\frac{y^2}{4K_y t}\right). \tag{2.11}$$

Assuming that the plume is vertically well-mixed, solving for the per-filament first moment requires a solution for c_1 satisfying the equation

$$\frac{\partial c_1}{\partial t} = U\mathrm{sgn}(y)c_0 + K_y \frac{\partial^2 c_1}{\partial y^2}. \tag{2.12}$$

We assume a form of $c_1 = fc_0$, where $f = f(y,t)$ gives the longitudinal per-filament centroid location as a function of time and lateral coordinate. Substituting fc_0 into the evolution equation for c_1, we get

$$\frac{\partial f}{\partial t} = u + K_y \frac{\partial^2 f}{\partial y^2} - \frac{y}{t}\frac{\partial f}{\partial y}. \tag{2.13}$$

This can be further simplified by non-dimensionalizing f by Ut, and assuming a similarity variable $\eta = y/\sqrt{4K_y t}$, such that $f/Ut = g(\eta)$ and the PDE is reduced to a second-order, variable-coefficient ODE in η:

$$g + \frac{\eta}{2}g' - \frac{g''}{4} - \mathrm{sgn}(\eta) = 0. \tag{2.14}$$

By symmetry $g(y=0,t)=0$. As y approaches $\pm\infty$ the motion of the centroid is independent of the shear at $y=0$ and carried only by the uniform flow, giving boundary conditions for f:

$$\lim_{y\to\pm\infty} f = \pm Ut \tag{2.15}$$

or equivalently

$$\lim_{\eta\to\pm\infty} g(\eta) = \pm 1. \tag{2.16}$$

The solution to (2.14), subject to the constraints at $y=0$ and (2.16) is then

$$g(\eta) = \sqrt{\pi}\eta \exp(\eta^2)\mathrm{erfc}|\eta|. \tag{2.17}$$

While g is both continuous and differentiable at $\eta = 0$, the second derivative is undefined at $\eta = 0$. While further manipulations are required to demonstrate that g is formally a weak solution to (2.14), we observe that g has exactly the expected behaviour, and precisely matches a numerical integration of (2.14).

Returning to the method of moments,

$$c_1 = c_0 Utg(\eta) \tag{2.18}$$

is substituted back into the cross-sectional integral of (2.7) to obtain an equation for the evolution of the second moment m_2. Applying (2.8), the time dependence of σ_x^2 for the infinite-domain, finite-shear case is reached:

$$\frac{\mathrm{d}\sigma_x^2}{\mathrm{d}t} = U^2 t + 2K_x. \tag{2.19}$$

Integrating in time from an initial point release we confirm the original quadratic scaling:

$$\sigma_x^2 = \tfrac{1}{2}U^2t^2 + 2K_xt. \tag{2.20}$$

As expected, the time dependence falls between the two previously discussed cases, with variance growing quadratically in time. Additionally, we observe that the quadratic case includes no dependence on the lateral dispersion coefficient K_y.

2.3. *Transitions*

The scaling arguments and results of the method of moments clearly delineate the behaviour of σ_x^2 in the simplified, 'pure' scenarios, but for a tracer cloud which passes through each regime (figure 1*d*) there is the additional question of how one regime transitions to the next. On further examination of (2.9), (2.10) and (2.19), we see that these transitions are characterized by a continuous $\mathrm{d}\sigma_x^2/\mathrm{d}t$.

Examining the evolution of σ_x^2 in the cubic case, (2.10), $\sigma_y^2 = 2K_yt$ describes the lateral variance and $\sigma_y = \sqrt{2K_yt}$ gives a linear scale for the lateral extent of the plume. When coupled with the shear this gives a scale for the range of velocities $U(t) \approx \partial u/\partial y\sqrt{K_yt}$. Equation (2.10) could then be rewritten as $\mathrm{d}\sigma_x^2/\mathrm{d}t \approx U^2(t)t$, similar to the first term in the quadratic evolution described by (2.19). The transition from cubic to quadratic is contained in the time dependence of the velocity scale, where the cubic regime implies a linear growth in U, and as the range of velocities asymptotes to a constant value the plume moves to the quadratic regime.

The transition from quadratic to linear dispersion can be examined in terms of the time scale for lateral mixing $T \sim W^2/K_y$. For $t > T$, the quadratic regime must be shut down and the dispersion reverts to the linear regime. Evaluating (2.19) with $t = T$ returns exactly the linear scaling, implying that the variance growth rate during the linear regime is also the maximum growth rate achieved by the quadratic regime.

More broadly, we can consider the generic scaling

$$\frac{\mathrm{d}\sigma_x^2}{\mathrm{d}t} \sim U^2(t)\tau(t), \tag{2.21}$$

where $U(t)$ is a velocity scale describing the range of velocities sampled by the plume and $\tau(t)$ is a time scale describing how long it takes for a parcel to sample that range of velocities. The three regimes can then be categorized by the time dependence in $U(t)$ and $\tau(t)$. In the cases where the lateral extent of the plume is not constrained by domain boundaries, the lateral mixing time grows with the plume size such that $\tau(t) \sim t$, but as the plume becomes large enough to 'feel' the constraints of the boundaries the time scale τ asymptotes to a constant value W^2/K_y, where W is the width of the domain. During periods when the plume has not yet sampled the full range of velocities in the flow, the lateral spreading and an assumed linear shear profile lead to $U^2(t) \sim t$. However, any finite flow has a finite range of velocities such that eventually U must also asymptote to a constant value. Combining the velocity and time scales, the resulting evolution of σ_x^2 is then clearly continuous, with time dependence ranging from t^2 when neither U nor τ have reached their asymptote, to a constant value in the linear shear dispersion limit of a constant U and τ.

2.4. *Effects of bathymetry*

In physical shoal–channel flows, as well as the example flow considered in § 4 below, lateral variation of the velocity field is typically correlated to depth variations. Sloping

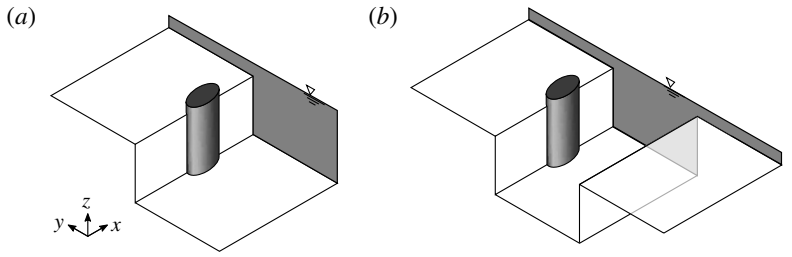

FIGURE 2. Schematic of plume interaction with bathymetry variability: (*a*) shelf bathymetry; (*b*) channel–shoal bathymetry.

regions of the lateral bathymetry profile act as partial lateral boundaries, and a scalar plume which extends over sloping areas would be partially bounded at depth. In this partially bounded state we might assume that the realized growth of σ_x^2 is best described by a combination of regimes. For the specific case of a vertically mixed plume centred on a break in the lateral bathymetry, such as in figure 2(*a*), the growth of variance is observed to remain purely quadratic in time. The quadratic growth scales in the same way as the flat-bottomed case, except with an attenuation factor which is a function of the ratio between the two depths. The derivation of this behaviour relies on an approximation that when the plume is centred on the step then solutions for the per-filament moments c_p are the same as for the flat-bottom case. The major difference from the flat-bottom case is that, with more tracer mass on the deeper side, the centroid is no longer stationary. To quantify, the plume variance c_1 is amended to described the per-filament first moment about the centroid rather than about the origin. Defining the centroid of the plume as $\mu_x = m_1/m_0$, this leads to an expression for the evolution of the variance,

$$\frac{\mathrm{d}\sigma_x^2}{\mathrm{d}t} = \left[\frac{4\alpha}{(\alpha+1)^2}\right] U^2 t + 2K_x, \tag{2.22}$$

where $\alpha \equiv H_s/H_c$, the ratio of the two depths. In essence the step bathymetry leads to an attenuated quadratic dispersion, where the attenuation factor is a function of the ratio between the two depths. In this special case of a plume centred on the bathymetric break and dispersed laterally by a constant eddy diffusivity, (2.22) compares favourably with particle tracking simulations. This case may be broadened slightly to also include a lateral variation in the lateral diffusion coefficient. In order for the plume to remain centred on $y = 0$ (i.e. c_0 has its maximum at $y = 0$), the distribution of mass must be asymmetric, with more mass and a broader lateral distribution on the side with higher lateral diffusivity. The effect is much the same as deepening one side, with an asymmetry in the mass distribution and a centroid which is no longer stationary. Pursuing the same approximate analysis, the combined effect falls into the same form as (2.22):

$$\frac{\mathrm{d}\sigma_x^2}{\mathrm{d}t} = \left[\frac{4\alpha\sqrt{\beta}}{(\alpha\sqrt{\beta}+1)^2}\right] U^2 t + 2K_x, \tag{2.23}$$

where $\beta \equiv K_{ys}/K_{yd}$, the ratio of the two lateral diffusion coefficients. In the general case, though, a plume offset from the break in bathymetry would then encounter that bathymetry as a partial boundary and the effective dispersion would be a mix

of regimes. Variation in the lateral diffusion coefficient that does not coincide with a maximum in c_0 would also cause a departure from this simplified case. Beyond the variation in lateral diffusion coefficient, deeper regions would also presumably see an increase in the longitudinal diffusion coefficient. This increase stems both from the simple increase in longitudinal turbulent mixing and from the variation in vertical shear dispersion between shallow and deep regions. In these more complex and physically realistic cases the dispersive behaviour is likely to be beyond the descriptive capacity of the present analytic solutions.

The numerical experiments of § 4 explore the dispersive behaviour of a range of plume releases in an idealized channel–shoal basin (figure 2*b*). In cases where the plume is initially positioned over the slope region, the above analysis suggests that once the plume expands beyond the shear region of the slope, σ_x^2 would grow with t^2. These numerical cases, though, include both sides of the channel. With sufficient time the plume will interact with both slopes, and proceed through a combination of linear and quadratic regimes and asymptote to a linear dispersion. We note, however, that just because a plume is not perfectly centred on a shear region does not mean that the quadratic regime is lost entirely. Rather, as long as there is a separation in time from when the plume mixes across a shear zone to the time that it encounters some feature bounding the lateral expansion, we expect a degree of quadratic growth.

3. Estimation of regimes and parameters

We next consider a number of particle plumes released in an idealized flow and analysed through the lens of the regimes discussed above. By careful evaluation of the time series of spatial moments we aim to discern: (i) the relative importance of each regime; and (ii) the degree to which the parameters of the simulated flow predict the evolution of the plume. The goal is then to describe the evolution of $\sigma_x^2(t)$ in terms of the three regimes and the relevant parameters, including the shear S, finite velocity range U, and lateral dispersion coefficient K_y. While the parameters of the regimes are generally changing in time, both due to the changing plume size and the local hydrodynamics driving the dispersion, the problem is simplified by considering the parameters to be constant over short windows of time. For each time window we expect that the time rate of change of the variance can be described by a second-degree polynomial

$$\frac{\mathrm{d}\sigma_x^2}{\mathrm{d}t} \approx \alpha_2 t^2 + \alpha_1 t + \alpha_0 \tag{3.1}$$

with the three coefficients corresponding conceptually to the three dispersion regimes. The presence of t and t^2 in (3.1) implies a time origin for the cubic and quadratic regimes. Since the plume behaviour should not depend on the choice of an absolute time origin, we must assume that t is instead relative to one or more time origins related to the plume state. One possible choice is to take all times relative to some t_y at which $\sigma_y^2 = 0$. However, as a plume shifts between regimes the x–y covariance of the plume may not evolve in lockstep with the lateral variance σ_y^2 and, as will be shown below, the covariance plays a key role in the time dependence of variance evolution.

Consider a pair of particles, such as in figure 3, in the finite shear flow of the quadratic regime, where one particle $\oplus$ is in the $y > 0$ half-plane and advected with a velocity $+U$, and the other, $\ominus$, is in the $y < 0$ half-plane advected with velocity $-U$. Ignoring for the moment effects of K_x and K_y, the longitudinal separation between

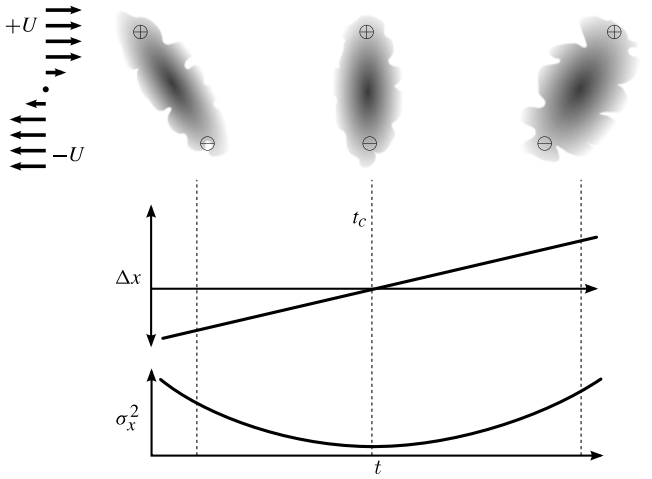

FIGURE 3. Accumulation of strain by a plume in the finite-shear, infinite-domain case.

the particles is then expected to evolve as $\Delta x = 2U(t - t_c)$, where t_c indicates the time when the particles are aligned across the flow (and more generally the time at which the covariance is zero). In the quadratic and cubic cases the particles are free to diffuse laterally without limit and on average never mix back across the shear region, which allows the approximation $\sigma_x \approx \Delta x/2$ (as opposed to the laterally bounded, linear regime where particles are periodically mixed back to the centre of the domain and this scaling does not hold). The variance then evolves as the square of time, and the time rate of change goes as $\mathrm{d}\sigma_x^2/\mathrm{d}t \sim U^2(t - t_c)$. Combining the t_c dependence from the present scaling argument with (2.19), we proceed with an adjusted form for the evolution of the variance,

$$\frac{\mathrm{d}\sigma_x^2}{\mathrm{d}t} \approx U^2(t - t_c). \tag{3.2}$$

In order to understand the independent effects of t_y and t_c in the cubic regime, we return to the method of moments. The previous analysis is modified in the choice of initial conditions for c_0, which now describes a laterally spreading Gaussian plume for which $\sigma_y^2(t = t_y) = 0$,

$$c_0(y, t) = \frac{m_0}{H\sqrt{4\pi K_y(t - t_y)}} \exp\left(-\frac{y^2}{2K_y(t - t_y)}\right). \tag{3.3}$$

For $t_y = t_c = 0$, (3.3) reduces to (2.11), the lateral mass distribution in both the cubic and quadratic analyses. The longitudinal concentration distribution is also modified such that $\mathrm{cov}_{xy}(t = t_c) = 0$. Condition $t_y < t_c$ indicates an offset in time between the start of lateral spreading and the start of straining. Subject to the initial and boundary conditions, and satisfying (2.6), the per-filament centroid is described by

$$c_1(y, t) = \frac{c_0 Sty}{2}\left(1 + \frac{t_c - t_y}{t - t_y}\right). \tag{3.4}$$

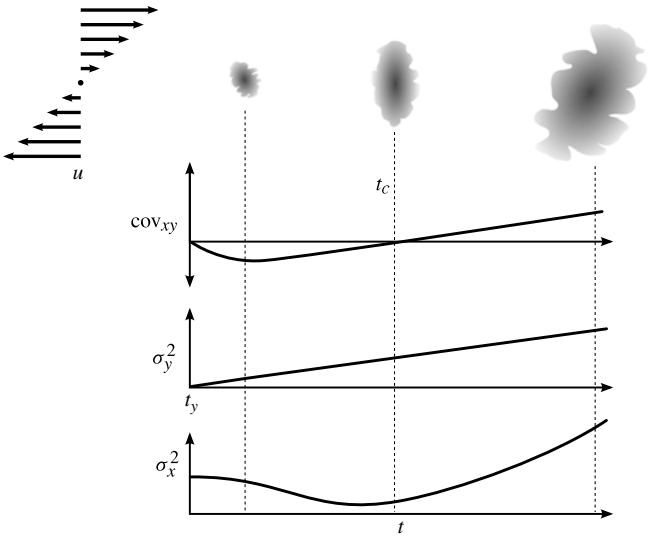

FIGURE 4. Relationship between σ_x^2 and the time origins for covariance and lateral variance in the case of infinite shear.

Applying (2.7), the evolution of the longitudinal variance is then given by

$$\frac{\mathrm{d}\sigma_x^2}{\mathrm{d}t} = 2K_y S^2 (t - t_c)(t - 2t_y + t_c) + 2K_x. \tag{3.5}$$

The schematic of figure 4 depicts the relationship among t_c, t_y, cov_{xy}, σ_y^2 and σ_x^2. Conceptually, $\sigma_y^2(t = t_c)$ dictates the initial range of velocities sampled by the plume and the covariance reflects an accumulation of strain in the plume, the same role as in the quadratic analysis above.

In moving from the pure, analytic cases of § 2 to the present forms which aim to be applicable to transitional states, it also becomes necessary to distinguish between the internal mixing of parcels within the plume, given by the dispersion coefficient K_y, and the lateral spreading of the plume, $\mathrm{d}\sigma_y^2/\mathrm{d}t$. In the unbounded case these are related by a factor of two, but as a plume becomes partially bounded or in the linear limit fully constrained by lateral boundaries $\mathrm{d}\sigma_y^2/\mathrm{d}t$ and K_y diverge. K_y continues to describe mixing within the plume but $\mathrm{d}\sigma_y^2/\mathrm{d}t$ tends towards zero. In the infinite-shear case we note that it is the lateral spreading of the plume which is relevant, and which should be attenuated when lateral boundaries play a role. Combining the time origins and replacing K_y with the more directly descriptive $\mathrm{d}\sigma_y^2/\mathrm{d}t$, we assume a form for the infinite-shear regime of

$$\frac{\mathrm{d}\sigma_x^2}{\mathrm{d}t} \approx \left(\frac{\partial u}{\partial y}\right)^2 \frac{\mathrm{d}\sigma_y^2}{\mathrm{d}t}(t - t_c)(t - 2t_y + t_c). \tag{3.6}$$

In the case of linear shear dispersion, for which the plume is laterally well-mixed, the lateral variance is by definition constant. The covariance in the linear dispersion case also asymptotes to a constant value with a time scale proportional to the lateral mixing time, after which the straining action of the shear is balanced by the homogenizing effect of lateral diffusion, shown schematically in figure 5. Corresponding to the lack of any evolving state in the linear case other than σ_x^2, there

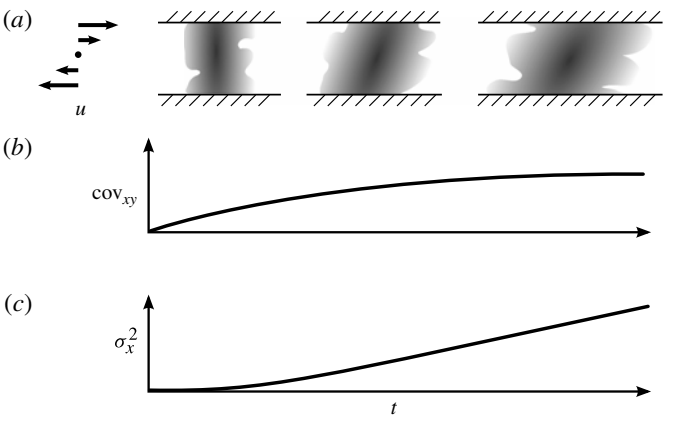

FIGURE 5. Asymptotic behaviour and lack of accumulated state for linear shear dispersion. (*a*) A sample tracer distribution, with corresponding time series of covariance (*b*) and longitudinal variance (*c*).

is no additional time dependence and no need to include t_c or t_y at times beyond the lateral mixing time, and the evolution of σ_x^2 remains

$$\frac{\mathrm{d}\sigma_x^2}{\mathrm{d}t} \approx \frac{U^2W^2}{\gamma K_y}, \tag{3.7}$$

where γ is a constant related to the specific velocity profile.

The simplest representation of the combined effects of the three regimes is then a simple summation of the individual contributions, taking into account the time origins for the higher-order regimes:

$$\frac{\mathrm{d}\sigma_x^2}{\mathrm{d}t} \approx \left(\frac{\partial u}{\partial y}\right)^2 \frac{\mathrm{d}\sigma_y^2}{\mathrm{d}t}(t-t_c)(t-2t_y+t_c) + U^2(t-t_c) + \frac{U^2W^2}{\gamma K_y}. \tag{3.8}$$

In order to make meaningful comparisons between observed coefficients of a polynomial fit as in (3.1) and (3.8) it becomes necessary to estimate t_c and t_y. Considering the effect of the time origins on each term, we connect the terms of (3.8) with the polynomial coefficients of (3.1). The highest order coefficient is unaffected by the time origins:

$$\left(\frac{\partial u}{\partial y}\right)^2 \frac{\mathrm{d}\sigma_y^2}{\mathrm{d}t} \approx \alpha_2. \tag{3.9}$$

Taking into account the time origins of the cubic dispersion term, the coefficient for t can then be approximated by

$$\left[U^2 - 2\left(\frac{\partial u}{\partial y}\right)^2 \frac{\mathrm{d}\sigma_y^2}{\mathrm{d}t} t_y\right] \approx \alpha_1. \tag{3.10}$$

Similarly, time origins for both the cubic and quadratic dispersion terms are relevant for the constant term of (3.1):

$$\frac{U^2W^2}{\gamma K_y} - U^2 t_c + \left(\frac{\partial u}{\partial y}\right)^2 \frac{\mathrm{d}\sigma_y^2}{\mathrm{d}t}(2t_c t_y - t_c^2) \approx \alpha_0. \tag{3.11}$$

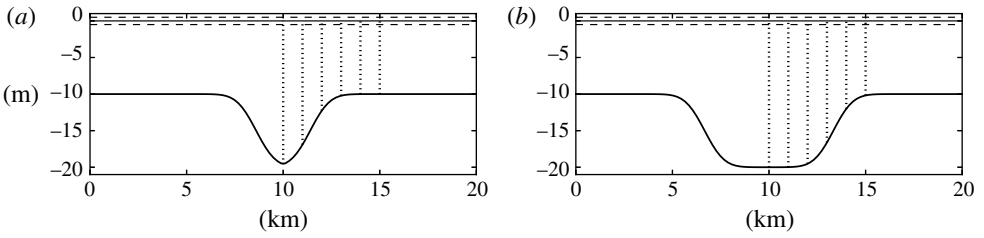

FIGURE 6. Bathymetry profiles for the two idealized domains. Horizontal dashed lines bracketing $z = 0$ denote the range of the tidal boundary condition. Vertical dotted lines denote particle release locations. (*a*) Narrow channel; (*b*) wide channel.

Note that (3.1), while including terms quadratic, linear and constant in time, does not map directly to the cubic, quadratic and linear shear dispersion regimes due to the time origins t_c and t_y. To more cleanly separate the influence of each regime, (3.9)–(3.11) are used to define a set of coefficients α_i^*, in terms of α_i, which describe the role of each individual regime:

$$\alpha_2^* = \alpha_2 \approx \left(\frac{\partial u}{\partial y}\right)^2 \frac{\mathrm{d}\sigma_y^2}{\mathrm{d}t}, \tag{3.12}$$

$$\alpha_1^* = \alpha_1 + 2\alpha_2 t_y \approx U^2, \tag{3.13}$$

$$\alpha_0^* = \alpha_0 + \alpha_1^* t_c - \alpha_2^*(2t_c t_y - t_c^2) \approx \frac{U^2 W^2}{\gamma K_y}. \tag{3.14}$$

With the effects of the time origins removed from each coefficient, we are left with a series of coefficients with one-to-one relationships with the three dispersion regimes and a prediction of each based on parameters of the flow.

4. Tidally forced channel–shoal domain

In a step towards applying the above analysis to real-world conditions we consider here a more realistic but still idealized flow. Two domains are utilized, both 100 km long and 20 km wide, varying in the lateral bathymetry profile as shown in figure 6. The $x = 0$ end of the channel is forced by 12 h periodic tides, with a peak-to-peak amplitude of 1.0 m, while at $x = 100$ km the landward end of the channel is closed. The hydrodynamic simulations utilize the SUNTANS RANS model (Fringer, Gerritsen & Street 2006), run in 2-D mode. The primary goal of these simulations is to drive a moderately complex but tractable two-dimensional flow field in which the three dispersion regimes may be simultaneously observed. Dimensions of the basin, tidal amplitudes and the lateral bathymetry profile fall within the range of typical physical values. We focus on the subtidal dispersion caused by interaction of the subtidal flow field with shorter-time-scale turbulent mixing and tidal stirring. The residual flow field is essentially the landward portion of the flow described by Li & O'Donnell (2005), in which the channel carries a residual landward flow and the shoals have a residual seaward flow.

4.1. *Particle tracking model*

We use FISH-PTM (Gross *et al.* 2011) to simulate the transport and dispersion of passive particles by the predicted hydrodynamic flow field output by SUNTANS.

This particle tracking model includes both deterministic transport by the Eulerian velocity field and a non-deterministic parameterization of turbulent dispersion. The non-deterministic component, a carefully formulated random walk, is calculated at each time, for each particle, according to the method of LaBolle *et al.* (2000), with a constant eddy diffusivity of $K_0 = 0.1\ \mathrm{m}^2\ \mathrm{s}^{-1}$. The diffusivity has been chosen to be relatively small so that transitions between regimes are sufficiently separated in time to allow a detailed analysis of each regime. We note that while the particle tracking model employs a constant eddy diffusivity, spatially varying dispersion within a tidal cycle (e.g. intratidal shear dispersion) is effectively a variable diffusivity at subtidal time scales. Though in the present cases we impose a constant, uniform and isotropic diffusivity, the method of LaBolle *et al.* (2000) allows for a simple treatment variable and discontinuous diffusivities, enabling simulation of the scenario discussed in § 2.4 in which the centre of the domain has both a break in bathymetry and a discontinuity in the diffusivity. The particle locations are updated via the following three-step process:

$$\boldsymbol{X}^{n+1/2} = \boldsymbol{X}^n + \boldsymbol{u}(\boldsymbol{X}^n)\Delta t, \tag{4.1}$$

$$\boldsymbol{X}^* = \mathrm{bounce}\{\boldsymbol{X}^{n+1/2}, \boldsymbol{R}\sqrt{2r^{-1}K_0(\boldsymbol{X}^{n+1/2})\Delta t}\}, \tag{4.2}$$

$$\boldsymbol{X}^{n+1} = \mathrm{bounce}\{\boldsymbol{X}^{n+1/2}, \boldsymbol{R}\sqrt{2r^{-1}K_0(\boldsymbol{X}^*)\Delta t}\}, \tag{4.3}$$

where $\boldsymbol{X}^n$ is a vector describing the particle location at step n, $\boldsymbol{u}(\boldsymbol{X})$ is the velocity from the hydrodynamic model, interpolated in time and space as needed, $\boldsymbol{R}$ is a random vector with components evenly distributed over $[-1, 1]$, and $r = 1/3$. To ensure that particles remain within the domain and do not accumulate at boundaries, they are reflected back into the domain, denoted by the bounce$\{\boldsymbol{X}, \boldsymbol{d}\}$ operator. If the segment $\overline{\boldsymbol{X}(\boldsymbol{X}+\boldsymbol{d})}$ intersects the boundary, then we define $s \in [0, 1]$ as the fraction of the original step before the first boundary collision: $\boldsymbol{X} + s\boldsymbol{d} \in \delta\Omega$. Then

$$\mathrm{bounce}\{\boldsymbol{X}, \boldsymbol{d}\} = \begin{cases} \boldsymbol{X} + s\boldsymbol{d} + (1-s)(\boldsymbol{d} - 2\hat{\boldsymbol{n}}(\boldsymbol{d}\cdot\hat{\boldsymbol{n}})) & \text{if collision} \\ \boldsymbol{X} + \boldsymbol{d} & \text{if path is free,} \end{cases} \tag{4.4}$$

where $\hat{\boldsymbol{n}}$ is the inward-facing normal of the boundary face at $\boldsymbol{X} + s\boldsymbol{d}$. The bounce method is applied iteratively to allow a single diffusion step to generate multiple boundary collisions and reflections, subject to the total length of the path with bounces being the same as the length of the original straight line path. Both the advective step and the diffusive step are subcycled as needed. The advective step is subcycled as particles cross an edge into a new cell of the hydrodynamic grid, and the diffusive step is subcycled according to the time-step constraints detailed in Ross & Sharples (2004).

Particle clouds are released, evenly distributed in the vertical, at several locations in both the lateral and longitudinal directions, shown in figures 6 and 7. The initial lateral position of the plume ranges from the centre of the channel to halfway between the channel centre and the lateral boundary of the domain. Each plume is tracked over 100 tidal periods. At the start of each tidal cycle the first and second moments are calculated as

$$\mu_j(t) = \frac{1}{N}\sum_{p=1}^{N} r_{p,j}(t) \tag{4.5}$$

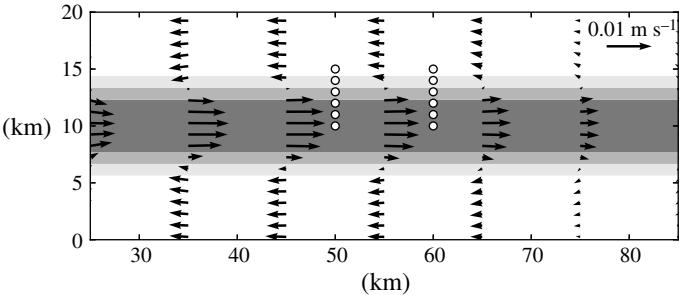

FIGURE 7. Plan view of the central portion of the wide channel idealized domain. Locations of particle plume releases are shown by empty circles, and the Lagrangian residual field is shown by arrows. Depth indicated by greyscale with breaks shown at depths of 11, 15 and 19 m.

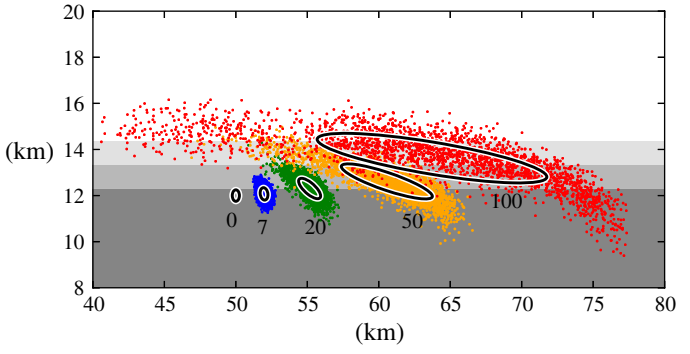

FIGURE 8. (Colour online) Instantaneous plume distributions after 0 (grey online), 7 (blue online), 20 (green online), 50 (orange online) and 100 (red online) tidal periods. Greyscale depth breaks at 11, 15, and 19 m, with the lower portion of the plot falling within the channel region and the upper half in the shoal region. Ellipses are drawn according to the 2-D covariance matrix.

and

$$\sigma_{jk}(t) = \frac{1}{N}\sum_{p=1}^{N}[r_{p,j}(t) - \mu_j(t)][r_{p,k}(t) - \mu_k(t)], \tag{4.6}$$

where $r_{p,j}(t)$ is the position of particle p along axis j at time t, N is the total number of particles and the indices j and k range over the coordinate axes x and y. With these definitions, $\sigma_x^2 \equiv \sigma_{xx}$, $\sigma_y^2 \equiv \sigma_{yy}$ and $\mathrm{cov}_{xy} \equiv \sigma_{xy}$.

In addition to tracking the evolution of each plume, the particle tracking model is also used to estimate a residual Lagrangian velocity field. This field is estimated by releasing particles on a uniform, 200 m grid throughout the domain, and extracting the displacement of each particle after being advected for exactly one tidal period with the dispersive random walk disabled. The displacements define the residual Lagrangian velocity, anchored in space at each respective initial position. The residual velocity field for the wide channel domain is shown by the arrows in figure 7 domain.

A sample plume trajectory is shown in figure 8, showing the interaction of the plume with slope-generated residual shear. The initial release is within the channel,

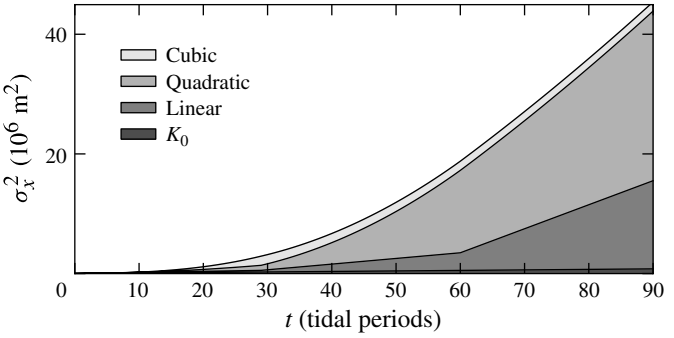

FIGURE 9. Cumulative growth of σ_x^2 for the same particle cloud as depicted in figure 8. The time series of σ_x^2 has been partitioned into the cumulative contributions of the three shear dispersion regimes, based on the observed values for α_i^*, plus the constant contribution of the imposed K_0.

close to the edge of the slope region. The initial residual transport carries the plume towards the closed end of the domain, while a mix of dispersion and lateral advection leads to a growing portion of the plume which samples the slope and shoal regions. Straining of the plume across the slope region leads to a significant quadratic growth in the variance. The time series of σ_x^2 is shown in figure 9, partitioned into contributions from the three dispersion regimes as well as the constant contribution from the imposed background dispersion rate K_0. The partitioning is shown as a stacked sum, corresponding to the terms of the summation

$$\sigma_x^2(t) = \int_0^t \alpha_2^*(\tau - t_c)(\tau - t_y)\,\mathrm{d}\tau \tag{4.7}$$

$$+ \int_0^t \alpha_1^*(\tau - t_c)\,\mathrm{d}\tau \tag{4.8}$$

$$+ \int_0^t \alpha_0^*\,\mathrm{d}\tau \tag{4.9}$$

$$+ \int_0^t 2K_0\,\mathrm{d}\tau, \tag{4.10}$$

where α_i^*, t_c and t_y are taken as constants within each of the three analysis windows (tidal periods 0–30, 30–60 and 60–90). From figure 9 one can see that the contribution from the cubic regime is relatively small, accumulated only in the very early spreading of the plume. The quadratic contribution is initially small, but between 30 and 90 tidal cycles this term contributes enough to variance growth to account for slightly over half the total variance growth. Only after 60 tidal cycles does the linear regime contribute significant variance, and ultimately accounts for ∼40 % of the total variance growth. The imposed internal mixing due to K_0 is a negligible source of longitudinal variance growth.

4.2. *Comparison of fit parameters to direct estimates*

In order to assess the relevance of the analytic regime descriptions to cases where the net dispersion is an evolving combination of multiple regimes, we compare the adjusted observed polynomial coefficients α_i^* with predicted quantities according

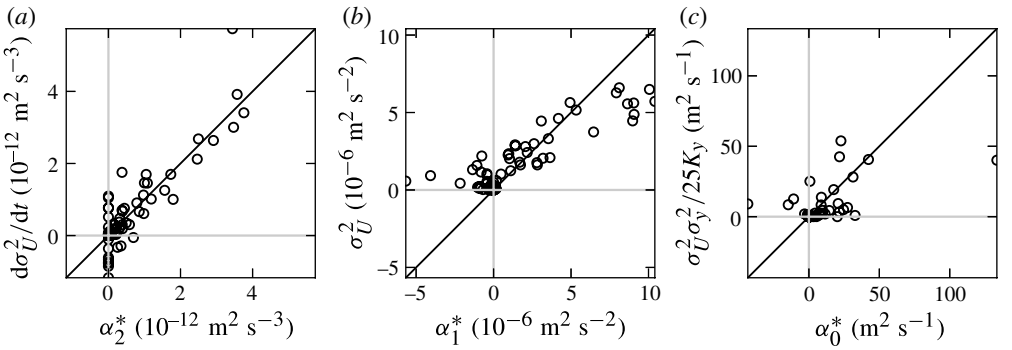

FIGURE 10. Correlation between predicted and observed growth coefficients. Diagonals show the 1:1 lines and grey perpendiculars intersect at (0, 0). Panels show correlation for (*a*) the infinite-shear regime, (*b*) the finite-shear/unbounded regime, and (*c*) the linear, Fickian limit of bounded-shear dispersion. Correlation coefficients are $R = 0.890$, 0.877 and 0.565 for α_2^*, α_1^* and α_0^*, respectively.

to (3.12)–(3.14). The predicted quantities depend on approximations of parameters describing the subset of the flow sampled by the plume during each time window. Within a single tidal cycle the internal dispersion is dominated by the imposed K_0 and for the estimates in this section we assume $K_x = K_y = K_0$. While the particle tracking results include tidal variations, we consider only the subtidal signals, obtained by extracting parameters only at integer tidal periods $t_n = nT$ where $T = 12$ h is the tidal period. The width scale $W(t_n)$ is approximated by $\sigma_y(t_n)$. The velocity scale $U(t_n)$ is extracted from the residual Lagrangian velocity field by taking the standard deviation σ_u of the residual along-channel velocity at each particle location at time t_n. Per-window quantities W and U are then taken as averages of $W(t_n)$ and $U(t_n)$ over all t_n in the time window. For the case of the quadratic coefficient in (3.12), we further simplify the approximation to a direct estimate of the rate of change of the range of velocities sampled by the plume. Assuming a uniform, constant shear $\partial u/\partial y$ in the vicinity of the plume (the base assumption for the cubic regime),

$$\left(\frac{\partial u}{\partial y}\right)^2 \frac{\mathrm{d}\sigma_y^2}{\mathrm{d}t} = \frac{\mathrm{d}}{\mathrm{d}t}\left(\frac{\partial u}{\partial y}\sigma_y\right)^2 = \frac{\mathrm{d}\sigma_u^2}{\mathrm{d}t}, \tag{4.11}$$

where the right-hand side is evaluated by fitting a line to the time series of σ_u^2 within each time window. The time origins t_c and t_y are estimated by a least-squares linear fit to time series of both cov_{xy} and σ_y^2 over the time window and solving for the time when the line crosses zero. In evaluating the polynomial fit (3.1) we further require that the leading quadratic coefficient be non-negative. While it is possible for a plume to exhibit growth described by a negative coefficient on t^2, the scaling relationships discussed here are not applicable to such flows. Flow features including longitudinal convergence or mean vorticity which rotates longitudinal variance into the lateral axis could lead to decreasing σ_x^2 but are beyond the present analysis.

A comparison of the measured α_i^* and corresponding predicted coefficients is shown in figure 10. Since the velocity shape factor γ is not one of the estimated parameters, for the purposes of the plotting we assume a nominal value of 25 but note that the slope of the correlation in figure 10(*c*) is arbitrary. The comparison for α_2^* (figure 10*a*) shows good agreement for larger observed values, but significant clustering around

0, largely due to the limitation that α_2 is required to be non-negative. Windows for which α_2 would have been negative if not constrained are most often times when the plume encounters some longitudinal variation in the flow. For example, plumes in the centre of the channel move slowly to the closed end of the basin and eventually encounter a significant longitudinal convergence, $\partial u/\partial x < 0$, compressing the plume and decreasing σ_x^2. A similar process occurs for plumes in the shoals which advect far enough towards to the open end of the domain to encounter the 'null' in the residual field. Both cases fall outside the range of regimes covered by the method of moments as applied in § 2, and a broader, fully two-dimensional approach would be required to adequately treat these cases. The lower correlation for α_0^* (figure 10*c*), relative to α_2^* and α_1^* (figure 10*a,b*), is due in part to variability of the velocity profile which is not captured by the constant value of γ. The fact that α_0^* relies on all three values of α_i, as well as linear and nonlinear terms in t_c and t_y undoubtedly contributes to the higher error relative to the higher-order α_2^* and α_1^*. Nonetheless, all three coefficients are significantly correlated to the predicted values, and the higher-order coefficients α_2^* and α_1^* are both well correlated and show good agreement in magnitude.

5. Discussion

The flows presented here have been purposely distilled down to cases where higher-order dispersive regimes may be observed and quantified. In observations or physically realistic simulations a broad range of processes leads to a more complex picture. In particular, varying bathymetry and velocity shear lead to temporal and spatial variability of K_y and K_x. The numerical simulations above employed a constant diffusivity in an effort to find reasonably complex flows which are not too far removed from the assumptions the analytic framework. The importance of these variations of course depends on the specifics of a particular domain and the time scales of interest to a particular application. In the context of subtidal dispersion, these dispersion coefficients parameterize the combined effects of numerous processes including turbulent mixing, longitudinal–vertical shear dispersion, tidal stirring and lateral–vertical shear dispersion. Variations in bathymetry undoubtedly contribute to variations in the turbulent mixing and vertical shear dispersion. Additionally, regions of high shear may have large-scale, semi-organized eddy structures with complex dispersive effects (Spydell & Feddersen 2012). We expect that the quadratic regime would be most evident in cases where the extent of regions of high variability (in bathymetry or eddy diffusivity) is small compared to the extent of the plume. Preliminary simulations and analysis in cases of simple variations in K_y show that the regime descriptions may still apply. However, with increasing heterogeneity in the diffusivity field we expect that transitions between regimes will become overlapped. With the diffusivities sampled by the plume changing in time, it may become difficult to isolate a particular regime and its parameters. Additional non-Fickian processes may also contribute to the overall plume dynamics, including residual density-driven transport in both longitudinal and lateral axes. Depending on the time scales involved, these processes may add to or mask high-order dispersion regimes. Further exploration of plume dispersion in physically realistic models, and with relaxed assumptions of variable diffusion, is necessary to better quantify the emergence and interaction of different dispersion regimes. However, there remains the fundamental notion that the velocity scale U present in shear dispersion relations cannot be assumed to asymptote to a constant value in the same time period as the lateral extent of the plume asymptotes to a constant value.

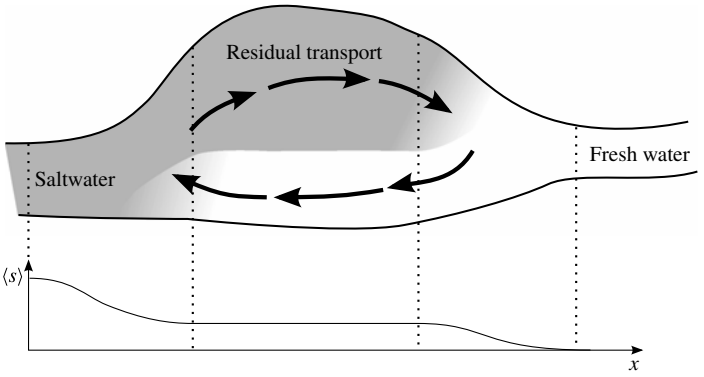

FIGURE 11. Flux view of quadratic dispersion in an estuarine reach which is not laterally well-mixed. Significant salt flux occurs even though gradients in the cross-sectionally averaged salinity $\langle s \rangle$ are negligible.

We note that the quantitative estimates for the importance of quadratic dispersion do not necessarily exclude periods of cubic dispersion, which when observed for a short period may exhibit a quadratic time dependence. Further examination of periods of significant quadratic dispersion, however, show little correlation between the measured quadratic and cubic terms, suggesting that dispersion in these periods is best classified as quadratic. Specifically, comparing α_2^* and α_1^* we find a correlation coefficient $R = -0.07$. A similar comparison, but between the predicted coefficients, shows a correlation coefficient of $R = 0.20$. Both comparisons reinforce the conceptual model of a plume quickly growing beyond the lateral scale of the shear and then reverting to a quadratic dispersion regime.

Of particular interest in the high-order regimes is that the overall dispersion, in terms of cross-sectionally averaged gradients and fluxes, is not Fickian. Operational one-dimensional models (e.g. Salah-Mars & McCann 2007) must make many simplifying assumptions, and the use of Fickian dispersion coefficients is one of them. While Fickian dispersion is easily expressed in terms of either plume growth ($\sigma^2 \approx 2Kt$) or a differentially defined flux ($F \approx -K(\partial C/\partial x)$), high-order dispersion regimes cannot be expressed in terms of local gradients. For the simplest, infinitely long, steady-state case one can argue that all time scales for lateral mixing are achieved and all dispersion reverts to linear Taylor dispersion. In more realistic applications, though, embayments are finite and often exhibit significant variation along the axis. One can imagine a situation such as figure 11 where a residual circulation transports salt through the embayment. In terms of a one-dimensional salt balance, though, gradients of the cross-sectionally averaged salinity $\langle s \rangle$ are negligible, even though the salt flux is quite significant. This situation is analogous to the quadratic dispersion regime in the sense that straining of the concentration field leads to significant dispersion or flux before lateral mixing is able to homogenize the cross-section.

6. Conclusions

Motivated by the structure of environmental flows, we have introduced a dispersion regime with quadratic dependence on time, to augment the previously studied cubic and linear dispersion regimes. This regime may be prevalent in flows where the lateral extent of the velocity shear is smaller than the lateral extent of the domain, such as

channel–shoal systems in which the slope features are narrow compared to the width of the channel or the total width of the basin. A plume with a lateral length scale falling between the width of the shear and the width of the domain is expected to evolve according to this quadratic regime. While simple scaling arguments quickly arrive at this behaviour, a more rigorous and precise description is obtained by way of the method of moments. In a suitably constructed idealized flow we find that all three regimes occur and that the net evolution of the plume variance can reasonably be predicted by parameters extracted from the flow.

Acknowledgement

This work has been financially supported by the California Coastal Conservancy and the National Science Foundation.

REFERENCES

ARIS, R. 1956 On the dispersion of a solute in a fluid flowing through a tube. *Proc. R. Soc. Lond.* A **235**, 67–77.

BARTON, N. G. 1983 On the method of moments for solute dispersion. *J. Fluid Mech.* **126**, 205–218.

FENG, S., CHENG, R. T. & XI, P. 1986 On tide-induced Lagrangian residual current and residual transport 2. Residual transport with application in South San Francisco Bay, California. *Water Resour. Res.* **22** (12), 1635–1646.

FISCHER, H. B., LIST, E. J., KOH, R. C. Y., IMBERGER, J. & BROOKS, N. H. 1979 *Mixing in Inland and Coastal Waters*. Academic.

FRINGER, O. B., GERRITSEN, M. & STREET, R. L. 2006 An unstructured-grid, finite-volume, nonhydrostatic, parallel coastal ocean simulator. *Ocean Model.* **14**, 139–173.

GROSS, E. S., MACWILLIAMS, M. L., HOLLEMAN, R. C. & HERVIER, T. A. 2011 *Particle tracking model: testing and applications report*. Study. Interagency Ecological Program, Berkeley, CA.

LABOLLE, E. M., QUASTEL, J., FOGG, G. E. & GRAVNER, J. 2000 Diffusion processes in composite porous media and their numerical integration by random walks: generalized stochastic differential equations with discontinuous coefficients. *Water Resour. Res.* **36** (3), 651–662.

LI, C. & O'DONNELL, J. 2005 The effect of channel length on the residual circulation in tidally dominated channels. *J. Phys. Oceanogr.* **35**, 1826–1840.

OKUBO, A. 1973 Effect of shoreline irregularities on streamwise dispersion in estuaries and other embayments. *Netherlands J. Sea Res.* **6** (1-2), 213–224.

ROSS, O. N. & SHARPLES, J. 2004 Recipe for 1-D Lagrangian particle tracking models in space-varying diffusivity. *Limnol. Oceanogr.: Methods* **2**, 289–302.

SAFFMAN, P. G. 1962 The effect of wind shear on horizontal spread from an instantaneous ground source. *Q. J. R. Meteorol. Soc.* **88** (378), 382–393.

SALAH-MARS, S. & MCCANN, M. W. Jr. 2007 Delta risk management strategy: water analysis module. *Tech. Mem.* URS Corporation, Oakland, CA.

SPYDELL, M. S. & FEDDERSEN, F. 2012 The effect of a non-zero Lagrangian time scale on bounded shear dispersion. *J. Fluid Mech.* **691**, 69–94.

STOMMEL, H. & FARMER, H. G. 1952 On the nature of estuarine circulation. *Tech. Rep*. Woods Hole Oceanographic Institution.

TAYLOR, G. I. 1953 Dispersion of soluble matter in solvent flowing slowly through a tube. *Proc. R. Soc. Lond.* A **219**, 186–203.

TAYLOR, G. I. 1954 The Dispersion of matter in turbulent flow through a pipe. *Proc. R. Soc. Lond.* A **223** (1155), 446–468.

YOUNG, W. R. & JONES, S. 1991 Shear dispersion. *Phys. Fluids* A **3** (5), 1087–1101.

YOUNG, W. R., RHINES, P. B. & GARRETT, C. J. R. 1982 Shear-flow dispersion, internal waves and horizontal mixing in the ocean. *J. Phys. Oceanogr.* **12**, 515–527.